Fully Passively Levitated Self-Bearing Machine Implemented within a Reaction Wheel

Joachim Van Verdeghem, *Member, IEEE,* and Bruno Dehez, *Senior Member, IEEE*

***Abstract*—Self-bearing machines offer a highly integrated solution to achieve the rotor drive and magnetic levitation within a single structure. Although the trend is toward a diminution in the number of actively stabilised degrees of freedom to reduce the requirement for sensors, power electronics and controllers, no self-bearing machine relying solely on passive phenomena has been successfully tested so far due to the restrictions highlighted by Earnshaw's Theorem. Recent researches have demonstrated, through electromechanical models and in-depth experimental investigations, that electrodynamic thrust self-bearing machines (EDTSBMs) can gather, within a combined winding, both the rotor axial passive suspension and motor functions. Nonetheless, the test rigs implementing them still comprised external means to ensure the rotor radial and tilt support. In this context, this paper takes the study of EDTSBMs to the final step by combining them with two permanent magnet centring bearings, yielding the first fully passively levitated self-bearing machines. A reaction wheel demonstrator based on the latter is designed and sized according to an optimal approach. Thorough experimental analyses dealing with the axial forces that support the rotor and its resulting axial position as well as the drive torque are carried out, notably proving that stable fully passive levitation can be achieved. Finally, the motor and suspension currents as well as the corresponding losses are investigated.**

***Index Terms*—Self-bearing motor, bearingless motor, electrodynamic, passive, levitation, magnetic bearing, combined winding**

I. Introduction

Self-bearing machines (SBMs), also referred to as bearingless machines, combine, within a single structure, the rotor drive with its magnetic suspension. Their intrinsic compactness notably renders them attractive and even essential in applications requiring to operate at high spin speeds. These advantages add to those inherent to the magnetic levitation, including the absence of lubrication, mechanical friction and thus wear, as well as the loss decrease. Nevertheless, to stabilise the five degrees of freedom linked to the rotor levitation, these machines require sensors, power electronics and controllers [1–4]. Aiming at reducing the system cost and complexity while increasing its reliability and compactness, the trend is towards a decrease in the number of actively stabilised degrees of freedom (DOFs). These latter are generally replaced with passive bearings relying on the interaction between either permanent magnets (PMs) only or PMs and ferromagnetic materials, as is the case with the axial and angular ones in slice machines [5–8] or the radial and angular ones in thrust self-bearing machines [9–13]. However, as stated by Earnshaw's theorem, the rotor cannot be levitated only with static magnetic fields, implying that alternative passive magnetic bearings (PMBs) should be implemented to achieve fully passive suspension [14].

Electrodynamic bearings (EDBs) belong to PMBs as they operate through the interaction between the magnetic field produced by permanent magnets and eddy currents induced in conductors due to their relative motion with respect to these PMs. They can either stabilise the radial DOFs, referred to as centring EDBs, or support the rotor along its spin axis, denoted electrodynamic thrust bearings (EDTBs). The former have been the subject of theoretical and experimental studies, underlining in particular that, unless significant external non-rotating damping is added to the system, the radial motion suffers from dynamic instability issues up to high rotor spin speeds [15–20]. Nevertheless, introducing such an important amount of damping in a contactless manner solely relying on passive phenomena remains an open problem [21, 22]. By contrast, EDTBs show stable operation in the conventional speed range, thus arousing a growing interest in the last fifteen years, both at the axial and radial flux configuration levels [23–25]. Although they could not be qualified as SBMs, fully passive magnetic levitations based on them have already been successfully implemented theoretically and experimentally [26–28]. Moreover, electromechanical models describing their rotor axial quasi-static and dynamic behaviours have been derived [28, 29]. The latter have later been extended to consider the five degrees of freedom related to the suspension, highlighting that, thanks to a specific connection of the windings, these bearings can also exert forces counteracting the rotor tilt [30].

Meanwhile, a first fully passively levitated self-bearing machine based on an EDTB has been proposed [31]. However, the latter was not operating due to the significant axial destabilising stiffness arising from the PM centring bearings. Furthermore, even though both the drive and the axial suspension shared the same PM arrangement, the armature winding comprised two separate sets of coils, each of them being devoted to one of these functions. Aiming at increasing

Manuscript received January 22, 2021; revised June 23, 2021; accepted July 19, 2021. Date of publication ...; date of current version .... Paper 2021-EMC-0081.R1, presented at the 2020 IEEE Energy Conversion Congress and Exposition, Detroit, MI, USA, Oct. 11-15, and approved for publication in the IEEE TRANSACTIONS ON INDUSTRY APPLICATIONS by the Electric Machines Committee of the IEEE Industry Applications Society. (Corresponding author: Joachim Van Verdeghem.)
The authors are with the Deparment of Mechatronic, Electrical Energy, and Dynamic Systems, Institute of Mechanics, Materials and Civil Engineering, Université Catholique de Louvain, Louvain-la-Neuve 1348, Belgium (e-mail: joachim.vanverdeghem@uclouvain.be; bruno.dehez@uclouvain.be).
Color versions of one or more of the figures in this paper are available online at http://ieeexplore.ieee.org.
Digital Object Identifier 10.1109/TIA....

the torque density while reducing the mechanical complexity, recent researches unveiled that EDTBs can generate both the drive torque and passive axial restoring forces within a single multifunction armature winding thanks to an appropriate connection to the power supply [32]. An electromechanical model allowing us to predict the rotor axial and spin dynamics of these electrodynamic thrust self-bearing (EDTSB) machines has also been derived and then validated through in-depth experimental investigations [33]. Later on, the operation principle of their tilt stabilising behaviour and the corresponding model have also been corroborated through measurements on a dedicated prototype [34]. Nevertheless, in both these test rigs, the radial degrees of freedom were supported through air bearings, the latter offering the advantage not to impact the motions and forces under study. This reveals that no fully passively levitated self-bearing machine has been designed, implemented and successfully tested so far.

In this context, this paper takes the development of EDTSB machines to the final step by investigating their combination with two permanent magnet centring bearings ensuring the rotor radial and tilt passive stabilisations [35]. A reaction wheel demonstrator, highlighting the interest and the feasibility of these fully passively levitated machines, is designed and sized following an optimal approach. The motor and passive suspension functions are experimentally characterised through the study of the axial forces, the underlying stiffness, the resulting rotor position, the drive torque as well as the corresponding currents and losses.

The paper is structured as follows. Section II describes the fully passively levitated motor structure as well as its operation principle. The electromechanical model governing the machine rotor dynamics is then outlined in Section III. Following on from this, Section IV presents the optimal approach adopted to size the reaction wheel. Section V is devoted to the description of the prototype and the test rig. Finally, the experimental characterisation is conducted in Section VI.

II. Structure & Principle

As illustrated in Fig. 1, the fully passively levitated machine considered in this study comprises two main subassemblies, namely the electrodynamic thrust self-bearing machine and the permanent magnet bearings, whose structure, purpose and operation principle are detailed hereinafter.

A. Thrust Self-Bearing Machine

1) Structure: As represented in Figs. 1(a) and 1(b), the thrust self-bearing machine can be either based on an axial flux [32] or a radial flux [25] configuration without having any impact on the operation principle. In both cases, the rotor comprises an arrangement of permanent magnets with alternate polarisation so as to produce a magnetic field featuring p pole pairs. The stator encompasses N identical and evenly distributed phases formed by the parallel connection of an upper and a lower winding, themselves consisting in p identical and evenly distributed coils connected in series. As

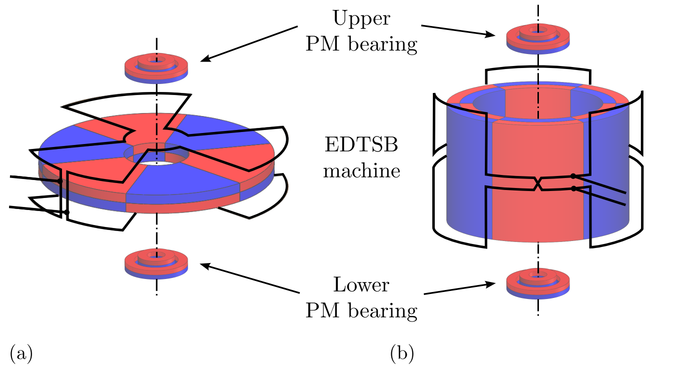

Fig. 1: Fully passively levitated machine (only one phase). (a) Axial flux configuration. (b) Radial flux configuration.

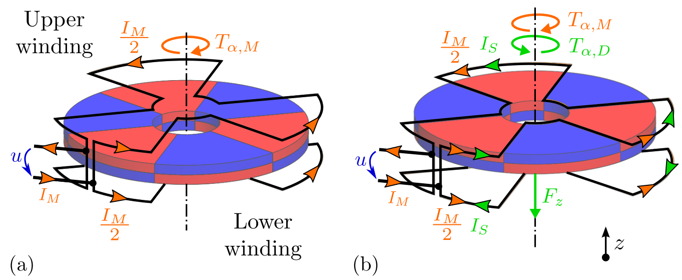

Fig. 2: Electrodynamic thrust self-bearing machine operation. (a) Centred position ($z = 0$). (b) Decentred position ($z \neq 0$).

described in [32], both these topologies can be implemented in various forms, that may include, e.g., ferromagnetic materials.

2) Principle: The electrodynamic thrust self-bearing machine ensures both the motor and rotor passive axial levitation functions. For the sake of clarity, the operation principle is solely studied on the basis of the axial flux configuration even if an identical analysis can be performed with the radial one.

On the one hand, when the rotor is axially centred, i.e. $z = 0$, the amplitudes Φ_U and Φ_L of the magnetic flux linkages due to the PMs respectively related to the upper and lower windings of each phase are identical. The resulting electromotive forces (EMFs) are therefore equal implying that the motor current I_M provided by the N-phase voltage source u follows a balanced distribution between these windings, as shown in Fig. 2(a). In accordance with Laplace's law, these currents generates a drive torque $T_{\alpha,M}$ by interacting with the axial PM magnetic field along the coil radial sections, as in a classic electrical machine, whereas their interaction with the azimuthal field component does not lead to an axial force since the upper and lower winding contributions to the latter compensate for each other.

On the other hand, when the rotor deviates from its nominal position, i.e. $z \neq 0$, the amplitudes Φ_U and Φ_L are no more equal and so are the EMFs. Hence, the motor current I_M is no longer evenly distributed between the upper and lower winding of each phase, as illustrated in Fig. 2(b). More precisely, the flux linkages having a linear dependence to the axial position z when considering small rotor displacements, one winding experiences an increase I_S of its current compared to the equilibrium while the second a decrease by an identical amount. The upper and lower winding currents I_U and I_L can therefore be construed as the superposition of the balanced motor current I_M, that comes from the power supply and passes through both windings in parallel, with a passively induced suspension current I_S, that circulates in the short-circuited path constituted by the series connection of both windings, these two currents being defined as:

$$\begin{cases} I_U = \dfrac{I_M}{2} + I_S \\ I_L = \dfrac{I_M}{2} - I_S \end{cases} \iff \begin{cases} I_M = I_U + I_L \\ I_S = \dfrac{I_U - I_L}{2} \end{cases}. \tag{1}$$

With regard to the forces, the PM magnetic flux density being divergence free, the linearity of the axial component with respect to the axial position implies the independence of the azimuthal component to the latter. Consequently, despite the rotor axial decentring, the motor current I_M still solely provides the drive torque $T_{\alpha,M}$. In contrast, thanks to a different path of circulation, the suspension current I_S interacts with the azimuthal PM magnetic field to produce an axial force F_z that tends to restore the rotor in its nominal position as well as with the field axial component, resulting in an undesirable drag torque $T_{\alpha,D}$ that goes against the motor torque $T_{\alpha,M}$.

Note that, in case of power supply failure, the self-bearing machine reduces to a conventional EDTB and therefore still provides the rotor axial suspension, ensuring a safe landing.

B. Permanent Magnet Bearings

The rotor radial and tilt stabilisations are achieved by two classic permanent magnet centring bearings placed on both sides of the machine. In accordance with Earnshaw's Theorem, in addition to the positive radial stiffness $k_{q,c}$, they also generate a negative destabilising axial stiffness $k_{z,c}$ that has to be compensated for by the thrust self-bearing machine to achieve the rotor stable levitation. Furthermore, for each bearing, the axial offset z_c separating both PM rings, respectively fixed to the stator and the rotor, when the rotor is in its nominal position, i.e. $z = 0$, can be adjusted to provide a force $F_{z,c}$ along that direction. In this way, these bearings can also act as axial load relievers, reducing or even cancelling the axial loads, such as the rotor weight, supported by the electrodynamic phenomena and therefore the underlying suspension currents I_S and losses. Although the vertical axis configuration is preferred, the self-bearing machine under study can also be operated horizontally. In this case, the radial stiffness $k_{q,c}$ has to be sufficient to balance the rotor weight within the radial stroke, unless an external magnetic compensator is implemented.

III. Electromechanical Model

Under the assumption of small displacements and considering a vertical axis configuration, the rotor six-degree-of-freedom dynamic behaviour, including its axial, radial and tilt stabilisations as well as its drive, can be described through the following set of nonlinear equations, as derived in [29, 30, 32] and experimentally validated in [32–34]:

$$\begin{cases} \ddot{q} = -\dfrac{C_q}{m}\dot{q} + \dfrac{F_{q,c}}{m} + \dfrac{F_{q,e}}{m} \\ \ddot{\beta} = -\dfrac{(C_\beta - \mathrm{j}\omega J_p)}{J_t}\dot{\beta} + \dfrac{T_{\beta,c}}{J_t} + \dfrac{T_{\beta,e}}{J_t} \\ \dot{F}_z = -\dfrac{2R}{L_{Sc}}F_z + \omega\left(\dfrac{T_{\alpha,D}}{z}\right) - \dot{z}\,\dfrac{(2K_z)^2N}{2L_{Sc}} \\ \dot{\left(\dfrac{T_{\alpha,D}}{z}\right)} = -\dfrac{2R}{L_{Sc}}\left(\dfrac{T_{\alpha,D}}{z}\right) - p^2\omega F_z - p^2\omega z\,\dfrac{(2K_z)^2N}{2L_{Sc}} \\ \ddot{z} = -\dfrac{C_z}{m}\dot{z} + \dfrac{F_z}{m} + \dfrac{F_{z,c}}{m} - g + \dfrac{F_{z,e}}{m} \\ \dot{I}_{M,d} = \dfrac{1}{L_{Mc}}u_d - \dfrac{R}{2L_{Mc}}I_{M,d} + p\omega I_{M,q} \\ \dot{I}_{M,q} = \dfrac{1}{L_{Mc}}u_q - \dfrac{R}{2L_{Mc}}I_{M,q} - p\omega I_{M,d} - \dfrac{p\omega K_\alpha}{L_{Mc}}\sqrt{\dfrac{N}{2}} \\ \dot{\omega} = \underbrace{pK_\alpha\sqrt{\dfrac{N}{2}}I_{M,q}}_{T_{\alpha,M}}\dfrac{1}{J_p} + \left(\dfrac{T_{\alpha,D}}{z}\right)\dfrac{z}{J_p} + \dfrac{T_{\alpha,e}}{J_p} \end{cases} \tag{2}$$

where $q = x + \mathrm{j}y$ and $\beta = \gamma - \mathrm{j}\lambda$ are the complex variables related to the rotor transverse and tilt dynamics, K_z is the flux gradient, i.e. the proportionality constant between the amplitude of the PM flux linkages and the axial position z, K_α is the motor flux constant, m is the rotor mass, J_p and J_t are the rotor polar and transverse moments of inertia, R is the winding resistance, $L_{S,c}$ and $L_{M,c}$ are the suspension and motor cyclic inductances, $I_{M,d}$ and $I_{M,q}$ are respectively the direct and quadrature-axis motor currents in the Park reference frame, u_d and u_q are the corresponding voltage applied to the armature winding, g is the acceleration due to gravity, $F_{q,c}$, $T_{\beta,c}$ and $F_{z,c}$ are the transverse, tilt and axial forces arising from the centring bearings, $F_{q,e}$, $F_{z,e}$, $T_{\beta,e}$ and $T_{\alpha,e}$ are the external forces and torques acting on the rotor and C_q, C_β and C_z are the external damping factors. The axial and

The first two equations are devoted to the rotor transverse and tilt dynamics and underline that their stabilisations is achieved through the permanent magnet centring bearings whereas the thrust self-bearing machine does not affect them. The following two equations, that describes the electrodynamic phenomena ensuring the passive axial suspension, are identical to those related to EDTBs alone and therefore do not depend on the motor current I_M. The fifth equation governs the rotor axial motion, notably taking into account the PM bearing and thrust self-bearing machine contributions as well as the gravity. The next two equations, that model the motor electrical behaviour in the Park reference frame, are similar to those characterising classic permanent magnet machines, thus being not affected by the rotor magnetic levitation and the underlying dynamics. Nevertheless, the last equation, dedicated to the spin motion, couples the rotor drive to the thrust bearing function through the drag torque $T_{\alpha,D}$, and conversely, via the rotor spin speed ω, the latter having a significant impact on the electrodynamic effects.

TABLE I: REACTION WHEEL SPECIFICATIONS

Parameter	Symbol	Unit	Value
Angular momentum	H	Nms	0.5
Dimensions	–	cm	$11 \times 11 \times 4$
Rated torque	$T^r_{\alpha,M}$	mNm	7.5
Rated consumption	P^r_t	W	≤ 12.5
Radial stiffness	$k_{q,c}$	N/mm	2.5
Tilt stiffness	$k_{\beta,c}$	mNm/deg	≥ 13.5

Under quasi-static conditions, i.e. $\dot{z} = \dot{\omega} = 0$, the axial electrodynamic stiffness k_z and the corresponding drag torque $T_{\alpha,D}$ can be retrieved from this model, yielding:

$$k_z = -\frac{F_z(\omega)}{z} = k_z^\infty \frac{(p\omega L_{S,c})^2}{(p\omega L_{S,c})^2 + (2R)^2}, \tag{3}$$

$$T_{\alpha,D} = -z^2 k_z^\infty \left(\frac{2R}{L_{S,c}}\right) \frac{p^2 \omega L_{S,c}^2}{(p\omega L_{S,c})^2 + (2R)^2}, \tag{4}$$

where k_z^∞ is the maximal stiffness, defined as:

$$k_z^\infty = \frac{(2K_z)^2 N}{2L_{S,c}}. \tag{5}$$

IV. OPTIMAL SIZING

This section presents the optimal approach followed to size the reaction wheel demonstrator. This application is particularly well suited for the fully passively levitated self-bearing machines under study. Indeed, the magnetic suspension allows to remove the drawbacks related to ball bearings such as the restriction on the spin speed, the stiction, the necessity for lubrication as well as the microvibrations coming from the rolling of the balls [4]. Moreover, these machines offer high compactness and reliability in comparison with active solutions thanks to the absence of sensors, power electronics and controllers dedicated to the rotor levitation. The relatively low stiffnesses generated by the passive phenomena are sufficient to support the rotor as the external forces are limited to those arising from the satellite slow dynamics imposed by these wheels. Considering an axial flux configuration, the thrust self-bearing machine rotor can also directly constitute the wheel itself thanks to its disc shape and to the high density of the permanent magnet material.

The specifications, summarised in Table I, have been retrieved from the technical data of two wheels operating with mechanical bearings (VECTRONIC AEROSPACE VRW-05 and BLUE CANYON TECH RWP500), except for those related to the stiffnesses that have been set based on existing bearingless machines. As with any component dedicated to a space application, the losses and the mass are key factors that have to be minimised. Indeed, the extraction of heat arising from the losses is only achieved through thermal radiation and is therefore limited whereas the mass directly impacts the launch cost. The optimisation process, that relies on an NSGA-II genetic algorithm, is conducted in two successive steps focusing respectively on the thrust self-bearing machine and the PM bearings. The mechanical and magnetic material properties considered in this study are presented in Table II.

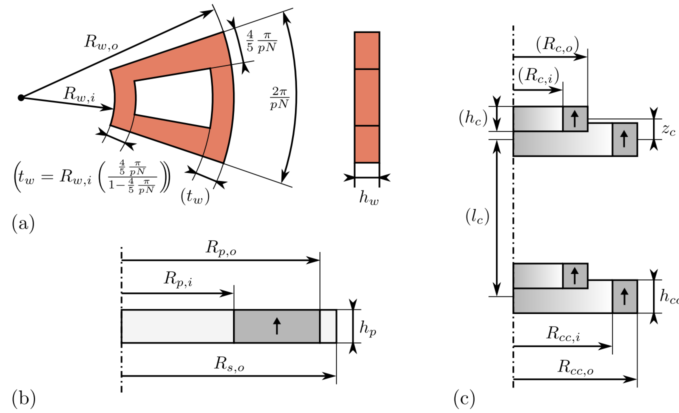

Fig. 3: Optimisation variables: machine geometry. (a) Coils. (b) Permanent magnet rotor. (c) Centring bearings.

A. Thrust Self-Bearing Machine

The thrust self-bearing machine, that ensures both the reaction wheel motor and passive axial stabilisation functions, relies on an axial flux ironless configuration. Aiming at simplifying the mechanical structure, no component is added to the permanent magnet rotor to store angular momentum. Lastly, the armature winding is constituted of non-overlapping concentrated coils so as to avoid large end-windings as well as to facilitate the manufacturing.

1) Parameters: The geometry of each coil depends on three independent parameters defined in Fig. 3(a). The number N of phases is set to three so that the self-bearing machine can be operated through a classic AC driver. The axial airgap is fixed to 1 (mm) to allow the rotor to deviate from its nominal position in reaction to external axial forces $F_{z,e}$ and angular torques $T_{\beta,e}$ without coming into contact with the windings. Regarding the rotor, as represented in Fig. 3(b), the wheel internal structure, the permanent magnet arrangement and the sleeve are fully described through four parameters. It should be stressed that all the structural components, such as the frame, are not taken into consideration since their masses do not depend on the machine internal dimensions. Finally, the optimisation variables also include the number p of pole pairs.

2) Problem Formulation: The self-bearing machine comprises neither stator conductive parts other than the windings nor ferromagnetic materials, thereby preventing eddy current and iron losses. The rotor does not experience any axial destabilising detent stiffness and cogging torque, both arising from the interaction between the permanent magnets and the stator, thanks to the ironless structure. The reaction wheel is intended to operate in space, leading to no windage losses. The armature reaction field is negligible due to the slotless stator and so are the resulting eddy currents in the permanent magnets. In the absence of external force $F_{z,e}$, the rotor stabilises in its equilibrium position, i.e. $z = 0$, resulting in no suspension power consumption. The total losses thus solely encompass the

TABLE II: OPTIMISATION - MATERIAL PROPERTIES

Parameter	Symbol	Unit	Value
Permanent magnet (NdFeB)			
Density	ρ_p	kg/m^3	7600
Tensile strength	$\sigma_{p,t}$	MPa	80
Compressive strength	$\sigma_{p,c}$	MPa	800
Remanent magnetisation	B_r	T	1.32
Wheel structure and sleeve (Titanium TA6V)			
Density	ρ_s	kg/m^3	4350
Poisson's ratio	ν_s	–	0.34
Yield strength	$\sigma_{s,y}$	MPa	850
Armature winding (Litz wire)			
Density	ρ_w	kg/m^3	4000
Resistivity (80°C)	–	Ωm	21×10^{-9}
Fill factor	–	–	0.4

copper losses related to the motor current I_M. Consequently, the problem consists in the minimisation of both the thrust self-bearing machine mass m_m and the Joule losses P_M^r generated under rated conditions while satisfying the constraints related to the specifications on the overall dimensions, the total power consumption P_t and the angular momentum storage H, the latter depending on the rotor maximal speed that is notably restricted by its structural integrity. The optimisation can therefore be formulated as follows:

$$\begin{aligned} &\underset{\{h_w, R_{w,i}, R_{w,o}, h_p, R_{p,i}, R_{p,o}, R_{s,o}, p\}}{\text{minimise}} && m_m \text{ and } P_M^r, \\ &\text{subject to} && H \geq 0.5 \text{ (Nms)}, \quad R_{s,o} \leq 50 \text{ (mm)}, \\ & && P_t^r \leq 12.5 \text{ (W)}, \quad h_t \leq 40 \text{ (mm)}. \end{aligned} \tag{6}$$

In practice, for each individual considered by the optimisation algorithm, the parameters of the model (2) that are required to evaluate the objective functions and constraints are identified. Specifically, the resistance R is determined through Pouillet's law whereas the suspension cyclic inductance $L_{S,c}$ as well as the flux gradient K_z and constant K_α are each independently calculated by means of 3D magnetostatic finite element simulations, following the methods described in [32].

a) Objective Functions: The mass m_m is determined on the basis of the material densities whereas the Joule losses P_M^r, that arise from the circulation of the quadrature axis motor current $I_{M,q}^r$ within the upper and lower windings connected in parallel, are obtained as:

$$P_M^r = \frac{R}{2} {I_{M,q}^r}^2. \tag{7}$$

This $q-$axis motor current $I_{M,q}^r$, that allows to produce the rated drive torque $T_{\alpha,M}^r$, can be easily retrieved from the electromechanical model defined in (2), yielding:

$$I_{M,q}^r = \frac{T_{\alpha,M}^r}{pK_\alpha\sqrt{\frac{3}{2}}}. \tag{8}$$

b) Constraints: The maximal angular momentum H that the reaction wheel can provide to the satellite to control its attitude directly depends on the rotor polar moment of inertia J_p, evaluated through the mass and dimensions of each of its components, as well as on the minimal and maximal spin speed ω_1 and ω_2 through:

$$H = J_p(\omega_2 - \omega_1). \tag{9}$$

In the absence of axial external force $F_{z,e}$, the minimal spin speed ω_1 is the one beyond which the rotor starts to levitate and thus corresponds to the static stability threshold, i.e. the speed that allow the electrodynamic effects to overcome the destabilising stiffness $k_{z,c}$ coming from the PM centring bearings, being calculated as [36]:

$$\omega_1 = \frac{1}{p}\frac{2R}{L_{Sc}}\sqrt{-\frac{k_{z,c}}{k_{z,c} + k_z^\infty}}. \tag{10}$$

The centring bearings comprising no ferromagnetic materials, Earnshaw's Theorem states that the axial negative stiffness $k_{z,c}$ can be deduced from its radial counterpart $k_{q,c}$, the latter being fixed by the specifications, through the following identity:

$$k_{z,c} + 2k_{q,c} = 0. \tag{11}$$

The reaction wheel maximal spin speed ω_2 is restrained by the rotor dynamic stability as well as its structural integrity. Regarding the former restriction, in the absence of external damping C_z, the axial motion becomes dynamically unstable as soon as the spin speed exceeds the one corresponding to the suspension electrical pole ω_e [36]:

$$\omega_e = \frac{1}{p}\frac{2R}{L_{S,c}}. \tag{12}$$

Concerning the latter restriction, the permanent magnet arrangement and the sleeve are the two limiting components. On the one hand, the stress distribution within one permanent magnet is evaluated through a 2D finite element simulation when subjected to the centrifugal effects and to a roller constraint on its outer diameter, representing the sleeve, as depicted in Fig. 4(a). The magnets being brittle, the principal normal stresses σ_r and σ_α are then compared to the corresponding material compressive and tensile strengths. Considering a safety coefficient of three, this allows to retrieve the highest speed that the magnets can withstand without breaking. On the other hand, the sleeve mechanical behaviour is analysed through a 2D analytical model derived under plane stress conditions [37]. The sleeve radial and azimuthal stresses are calculated assuming that, as illustrated in Fig. 4(b), the inner diameter is subject to a uniform stress $\sigma_p(\rho_p\omega^2)$ that arises from the contact of the PM due to the centrifugal effects, the latter also acting on the sleeve. The sleeve being made of a ductile material, the resulting Von Mises stress σ_{VM} is compared to the yield strength to determine the maximal speed that can be reached without compromising its integrity.

As regards the constraint on the rated consumption, the motor Joule losses being the only ones generated within the machine, the total power P_t^r required to produce the rated

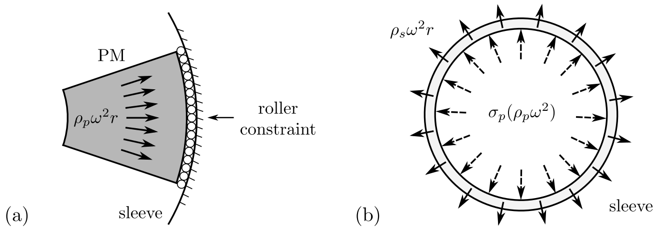

Fig. 4: Optimisation: structural models. (a) PMs. (b) Sleeve.

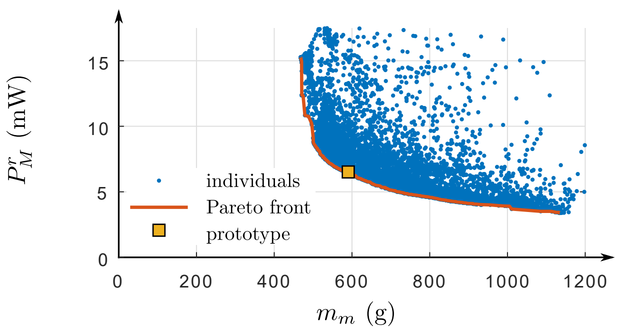

Fig. 5: Thrust self-bearing machine optimisation results.

torque $T^r_{\alpha,M}$ at the maximal rotor spin speed ω_2 amounts to:

$$P_t^r = P_M^r + \omega_2 T^r_{\alpha,M}. \tag{13}$$

3) Results: Fig. 5 shows the optimisation results, the dots corresponding to the evaluated individuals that respect the constraints, the solid line to the resulting Pareto front and the square to the individual based on which the prototype is manufactured. The latter is selected in the knee region, thus offering a trade-off between both objective functions along with a reasonable number of pole pairs p so as to facilitate the winding of the coils. This specific machine, whose parameters are listed in Table III, provides a maximal angular momentum H equal to 0.52 (Nms) between 5150 and 14 000 (rpm) for a rated total power consumption maintained below 11 (W). Regarding the rotor structural behaviour, Fig. 6 illustrates the evolution with the radial position r of the stresses σ arising from the centrifugal load exerted at the maximal speed. It can be observed that the principal stresses σ_r and σ_α acting in the permanent magnets are below the material compressive and tensile strengths. In contrast, considering the safety coefficient of three, the equivalent Von Mises stress σ_{VM} at the inner radius of the sleeve, that mainly results from the tangential component, reaches the yield strength. This highlights that the maximal speed ω_2 is limited by the sleeve in the selected optimised design. The radial component of the displacement field does not exceed 65 (μm) at this speed.

B. Permanent Magnet Bearings

1) Parameters: As represented in Fig. 3(c), the permanent magnet bearings, that ensure the rotor radial and tilt passive stabilisation, are fully characterised through eight parameters. Among them, the dimensions of the rotating rings are fixed

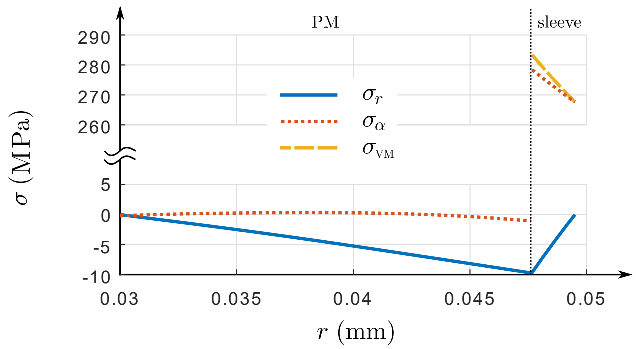

Fig. 6: Evolution of the stresses σ with the radial position r in the permanent magnets and the sleeve.

TABLE III: Optimisation - final parameters

Parameter	Symbol	Unit	Value
Airgap	e	mm	1
Number of phases	N	–	3
Number of pole pairs	p	–	8
Winding height	h_w	mm	4.2
Winding inner radius	$R_{w,i}$	mm	29.4
Winding outer radius	$R_{w,o}$	mm	49.7
PM height	h_p	mm	9.5
PM inner radius	$R_{p,i}$	mm	30
PM outer radius	$R_{p,o}$	mm	47.7
Sleeve outer radius	$R_{s,o}$	mm	49.5
Rotating ring height	h_c	mm	1.5
Rotating ring inner radius	$R_{c,o}$	mm	4.5
Rotating ring outer radius	$R_{c,i}$	mm	6
Bearing axial distance	l_c	mm	36.2
Stationary ring height	h_{cc}	mm	1.8
Stationary ring inner radius	$R_{cc,o}$	mm	7.6
Stationary ring outer radius	$R_{cc,i}$	mm	11.5
Axial offset	z_c	mm	0.7

since these magnets have been selected in the supplier stock to lower the prototype cost. The axial distance l_c between both centring bearings is held as wide as possible within the range allowed by the specification on the machine length so as to obtain the highest tilt stiffness $k_{\beta,c}$. As stated in Section VI-B, these bearings can also provide, through the adjustment of the axial offset z_c that separate their rings, an axial force $F_{z,c}$ allowing to compensate for constant loads exerted on the rotor. Although the reaction wheel is intended to operate in space, this parameter, and therefore the underlying force, is not set to zero as the rotor weight has to be counterbalanced to perform the experimental characterisation under similar conditions. Hence, the optimisation variables comprise the three stationary ring dimensions and the axial offset z_c.

2) Problem Formulation: The PM centring bearings generating no losses, the optimisation problem reduces to the minimisation of their mass m_c while complying with the constraints related to the load relieving force $F_{z,c}$, that has to be sufficient to support the rotor weight, and the specifications on the stiffnesses:

$$
\begin{aligned}
\underset{\{z_c,h_{cc},R_{cc,i},R_{cc,o}\}}{\text{minimise}} \quad & m_c, \\
\text{subject to} \quad & F_{z,c}(z_c) = mg, \\
& k_{q,c}(z_c) = 2.5 \text{ (N/mm)}, \\
& k_{\beta,c}(z_c) \geq 13.5 \text{ (mNm/deg)}.
\end{aligned} \tag{14}
$$

The objective function is evaluated on the basis of the material density. Regarding the constraints, the destabilising axial force $F_{z,c}$ and the torque $T_{\beta,c}$ counteracting the rotor tilt are obtained respectively through static 2D axisymmetric and 3D finite element simulations, the corresponding stiffnesses being retrieved from them, whereas, in accordance with Earnshaw's Theorem, the radial stiffness $k_{q,c}$ is directly deduced from its axial counterpart $k_{z,c}$ through (11).

3) Results: The bearing optimal configuration, whose dimensions are listed in Table III, features a mass m_c and a tilt stiffness $k_{\beta,c}$ respectively equal to 7.5 (g) and 13.6 (mNm/deg).

V. Experimental Setup

This section describes the prototype as well as the dedicated test rig allowing us to study, characterise and validate the fully passive magnetic suspension based on an electrodynamic thrust self-bearing machine.

A. Prototype

Figs. 7(a) and 7(b) show respectively a picture and a cross-sectional view of the fully passively levitated reaction wheel prototype. As represented in Fig. 7(c), the upper and lower armature windings of the thrust self-bearing motor comprise each $pN = 24$ coils (1) that are fixed on the non-magnetic non-conductive frame (2) and connected through printed circuit boards (3) to form the three phases. Each of these coils is constituted of 16 loops wound from 1 (mm) diameter Litz wire, thus preventing the appearance of locally induced Eddy currents. It should be noted that, as proved in [33], external inductors can be connected in series with each phase to improve the electrodynamic stiffness at small speeds. The rotor, depicted in Fig. 7(d), is composed of a non-magnetic stainless steel shaft (4) on which the self-bearing motor PM arrangement (5) as well as the rotating permanent magnet rings (6) of both centring bearings are attached. The corresponding stationary rings (7) being fixed on threaded parts (8) that screw on the frame (2), their axial positions can be adjusted so as to tune the total axial load relieving force $F_{z,c}$ and the underlying stiffness $k_{z,c}$. The latter being negative, the electrodynamic phenomena can not ensure the rotor stable axial levitation from zero spin speed. Thence, two landing bearings, each consisting in a ceramic ball (9), fixed to one shaft end, that can rotate on a stainless steel plate (10), are placed on both sides of the machine. These plates are themselves fastened to a threaded part (11) screwing on the frame (2) so that the rotor axial stroke can be adapted. Two balls bearings (12), whose bore is larger than the shaft diameter, serve as radial

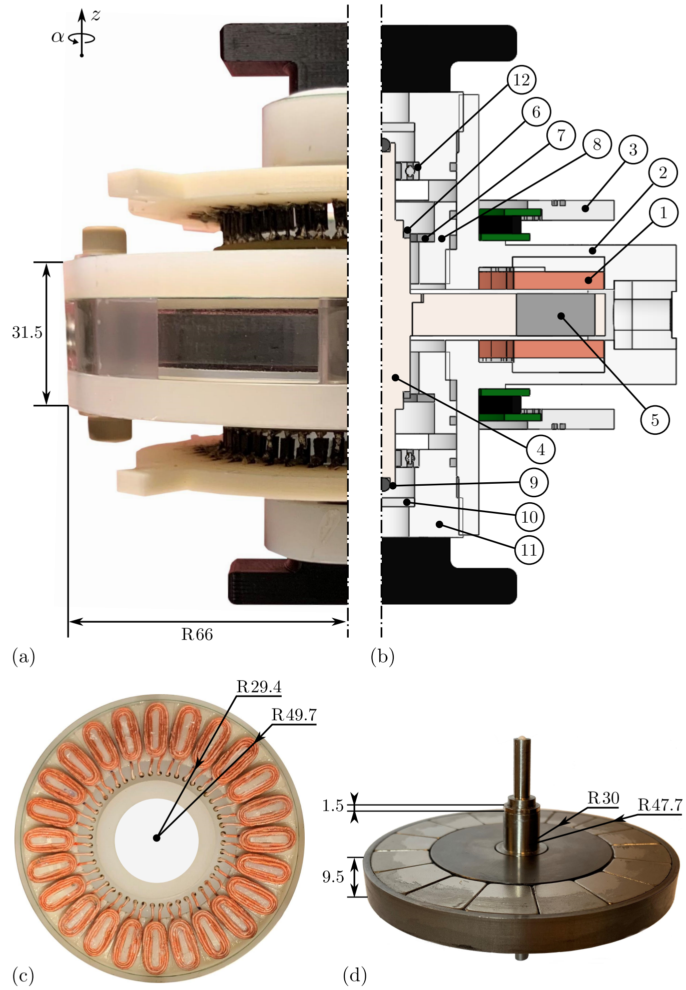

Fig. 7: Fully passively levitated machine prototype. (a) Picture. (b) Cross-sectional view. (c) Armature winding. (d) Rotor.

safety bearings in case of instability or failure. No external non-rotating damping is added to the system. Indeed, unlike their centring counterparts, the EDTSB machines does not require it to achieve stable rotor magnetic suspension. Finally, let us point out that the prototype operates without any sensor since the rotor levitation is achieved solely through passive phenomena and its spin speed is controlled with a sensorless AC driver (Texas Instruments DRV8312EVM).

B. Test Rig

The test rig instrumentation comes in two different configurations, allowing us to study either the permanent magnet bearings or the thrust self-bearing machine.

In the first case, as depicted in Fig. 8(a), the axial force $F_{z,c}$, arising from one or both centring bearings, is measured with a force sensor (1) (Lorenz M-2416) attached to the rotor lower shaft end through a rigid coupling (2). This sensor being itself fixed to a three-axis linear stage (3), the rotor radial position can be accurately set so as to ensure the concentricity between both PM rings constituting each bearing before a sweep is performed in the axial direction. Let us point out

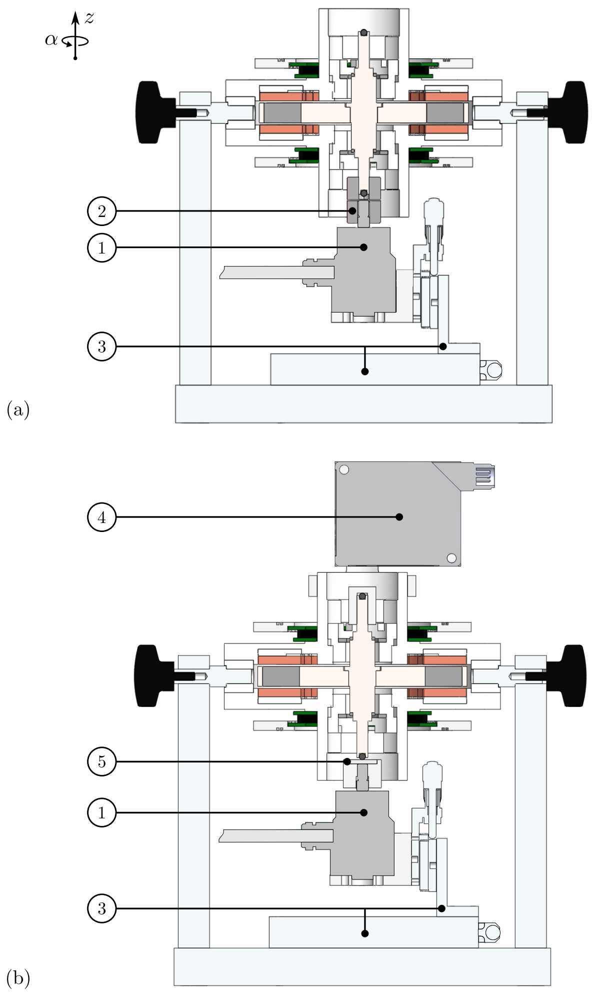

Fig. 8: Test rig. (a) Permanent magnet bearing characterisation. (b) Thrust self-bearing machine characterisation.

that, in accordance with Earnshaw's Theorem, the positive radial stiffness $k_{q,c}$ generated by these bearings can be directly deduced from the axial counterpart $k_{z,c}$ through (11).

Regarding the self-bearing motor characterisation, as represented in Fig. 8(b), a laser displacement sensor 4 (SICK OD2-P30W04I0) provides a high precision measurement of the rotor axial position z whereas its spin speed ω is estimated through the frequency of the voltage taken across the motor terminals. The force sensor 1, on which a stainless steel plate 5 is mounted, serves as lower landing bearing while gauging the normal force $F_{z,n}$ resulting from the rotor contact. Finally, the currents I_U and I_L flowing in the upper and lower windings of each phase are acquired by means of current clamps.

VI. Experimental Characterisation

This section is dedicated to the experimental characterisation of the motor and levitation functions of the reaction wheel demonstrator. Specifically, it deals with the thrust self-bearing machine, the permanent magnet bearings and the resulting fully passive suspension. Although the wheel has

TABLE IV: Model parameters

Parameter	Symbol	Unit	Value
Rotor mass	m	g	500
Rotor polar inertia	J_p	gm^2	0.647
Number of phases	N	–	3
Number of pole pairs	p	–	8
Flux gradient	K_z	Wb/m	0.78
Flux constant	K_α	mWb	3.31
Suspension cyclic inductance	$L_{S,c}$	μH	38.4
— with external inductors	$L_{S,c}$	μH	134.4
Motor cyclic inductance	$L_{M,c}$	mH	1.008
— with external inductors	$L_{M,c}$	mH	1.033
Winding resistance	R	mΩ	407
— with external inductors	R	mΩ	415
Axial external damping	C_z	Ns/m	0

been designed to operate up to 14 000 (rpm), this experimental characterisation is limited to 6000 (rpm) due to safety requirements and constraints imposed by the AC driver. Note that this does not impact the observations that can be drawn since, as will be shown hereinafter, the rotor axial behaviour does not significantly vary beyond this speed.

A. Thrust Self-Bearing Machine

1) Parameter Identification: The six equations allowing us to predict the thrust self-bearing machine currents, the underlying forces as well as the resulting spin and axial dynamics depend on ten parameters, among which seven still have to be identified. The rotor mass m is measured through a scale whereas the polar moment of inertia J_p is calculated via a CAD software. The suspension and motor cyclic inductances $L_{S,c}$ and $L_{M,c}$ as well as the winding resistance R are evaluated, with and without the additional external inductors, by means of a LCR meter. It should be noted that, the motor inductance $L_{M,c}$ being low, 1 (mH) chokes are connected in series with the three-phase power supply to reduce the current ripple, without having any impact on the axial suspension. The flux gradient K_z and constant K_α are extracted from the analysis of the evolution with the axial position z of the upper and lower flux linkage amplitudes, themselves being retrieved from the corresponding back electromotive forces [33]. More precisely, the former parameter corresponds to their slopes whereas latter to the flux linked at their intersection. Table IV summarises the model parameters.

2) Electrodynamic Stiffness & Force: Fig. 9 illustrates the evolution of the electrodynamic stiffness k_z, predicted through the theoretical equation (3), with the spin speed ω, the solid and dotted lines corresponding respectively to the case without and with the external inductors. As expected, their addition significantly improves the stiffness at small speeds by reducing the electrical pole [33]. In this way, the speed from which the rotor starts to levitate lessens. Nevertheless, the speed $\omega_e = 2R/(pL_{Sc}) = 7325$ (rpm) related to the electrical pole also represents the threshold beyond which the axial motion encounters a dynamic instability in the absence of

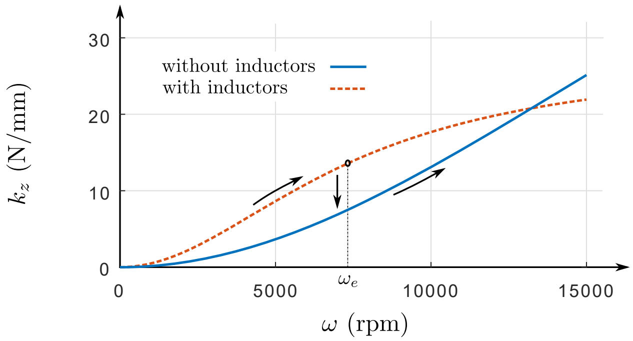

Fig. 9: Evolution of the electrodynamic stiffness k_z according to the spin speed ω with and without the additional inductors.

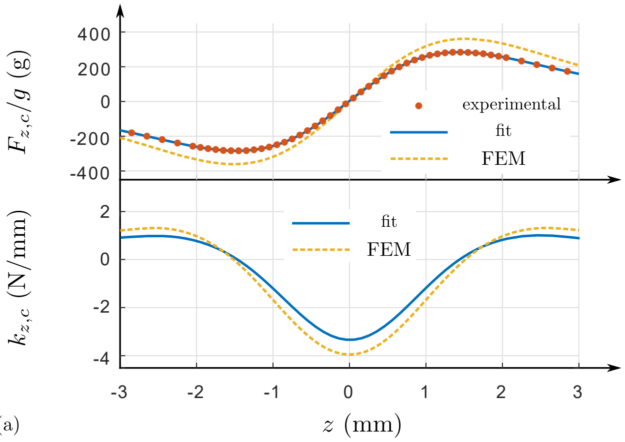

(a)

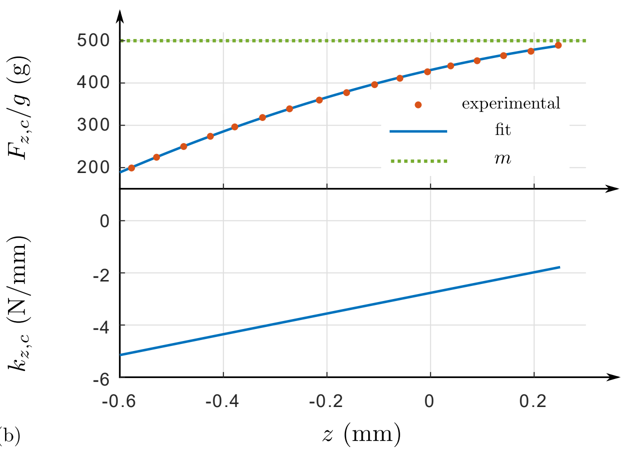

(b)

Fig. 10: Evolution of the axial force $F_{z,c}$ and the underlying stiffness $k_{z,c}$ with the axial position z. (a) One centring bearing. (b) Both centring bearings.

non-rotating damping C_z [36]. Thence, to reach higher speeds and meet the specification regarding the momentum storage, these additional inductors should be short-circuited around 7000 (rpm), the stiffness declining from 13 to 7 (N/mm). Finally, without the inductors, increasing the spin speed should allow us to reach up to 23 (N/mm) at 14 000 (rpm). The force capability of the prototype can be obtained based the electrodynamic stiffness k_z and the maximal admissible rotor axial stroke, fixed to 0.75 (mm), through (3) while taking the force $F_{z,c}$ due to the permanent magnet bearings into account.

B. Permanent Magnet Bearings

Fig. 10(a) shows the evolution of the axial force $F_{z,c}$ produced by a single centring bearing with the axial deflection z as well as the underlying stiffness $k_{z,c}$. The discrepancy between the finite element model and the experimental data comes from the uncertainty on the remanent magnetisation, the relative permeability set to one in simulation and the inaccuracy of the PM dimensions, this effect being exacerbated by the non-negligible relative coating thickness. As stated in Section VI-B, the axial offset separating both rings of each bearing can be adapted so as to tune the total axial force $F_{z,c}$ generated in the rotor nominal position, i.e. $z = 0$. Rather than counterbalancing the entire weight, a specific bearing adjustment leading to a partial compensation is chosen for the fully passive suspension characterisation. In this manner, the force $F_{z,n}$ arising from the contact between the rotor and the lower landing bearing is significant until the takeoff and so is the suspension current I_S throughout the levitation, thus facilitating their measurement and analysis. More precisely, the upper and lower centring bearing offsets are respectively set to 1.435 and 0.45 (mm), the former providing a high force as well as a low stiffness and vice versa for the latter. Fig. 10(b) illustrates the resulting axial load relieving force $F_{z,c}$ and the underlying stiffness $k_{z,c}$. As expected, the force is positive regardless of the axial position z, thus acting against the rotor weight. By contrast, the axial stiffness $k_{z,c}$ is negative and has thence to be balanced by the electrodynamic effects to allow for rotor stable levitation. Let us finally point out that the corresponding radial stiffness $k_{q,c}$, deduced with Earnshaw's Theorem through (11), decreases from 2.5 to 0.9 (N/mm) along the considered axial stroke.

C. Fully Passive Suspension

Let us now carry out a thorough investigation of the fully passively levitated self-bearing machine, encompassing in particular the analysis of the rotor axial position, the force distribution, the underlying stiffness, the drive torque, the motor and suspension currents as well as the drag losses. To that end, a specific sequence consisting of the machine start-up, the rotor being accelerated in two steps from 0 to 6000 (rpm), followed by the disconnection of the driver from the armature winding, thus reducing the machine to a conventional EDTB, is studied hereinafter.

1) Axial Position & Force Distribution: Fig. 11 represents the time evolution of the rotor spin speed ω, its axial position z and the three axial forces counteracting its weight, namely the electrodynamic force F_z, the load relieving force $F_{z,c}$ coming from the PM centring bearings and the normal force $F_{z,n}$ resulting from the contact with the lower landing bearing. Among these forces, the former two are respectively predicted through the theoretical expression (3) and obtained by combin-

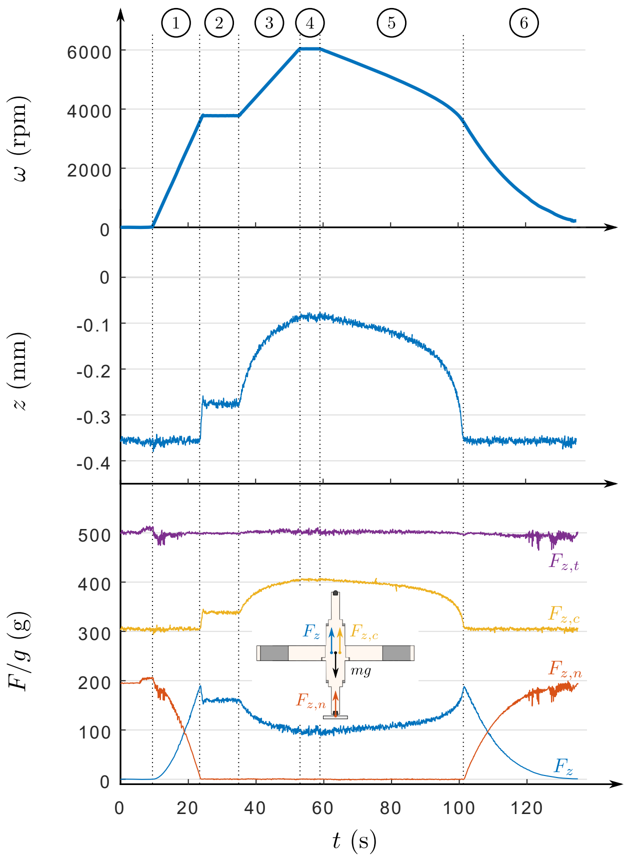

Fig. 11: Time evolution of the rotor spin speed ω, axial position z and the three axial forces counteracting its weight, namely the electrodynamic force F_z, the load relieving force $F_{z,c}$ and the contact force $F_{z,n}$.

ing the axial position measurement with the characterisation of the centring bearing pair performed in Section VI-B while the latter is directly retrieved from the axial force sensor.

As long as the machine is at standstill, the rotor lies on the lower landing bearing, located at $z = -0.357$ (mm), the latter supporting approximately 195 (g) while the remainder of the rotor mass, i.e. 305 (g), is provided by the load relieving force $F_{z,c}$. As will be shown in Section VI-C3, before the machine start-up, the sensorless AC driver carries out a step of direct-axis motor current $I_{M,d}$ to estimate the winding resistance. The impedances of the upper and lower windings being not exactly identical, this current induces a 10 (g) leap in the normal force $F_{z,c}$. Let us however point out that, in the rest of the sequence, the $d-$axis current is controlled with a setpoint equal to zero, thus no longer generating any parasitic axial force.

During step 1, while the axial position z and therefore the load relieving force $F_{z,c}$ remain constant, the electrodynamic force F_z increases with the spin speed raise, thus unloading the landing bearing whose contact force $F_{z,n}$ follows the exact opposite trend up to reach zero. At that particular point, corresponding to a spin speed equal to 3600 (rpm) and marking the onset of step 2, the rotor takes off from

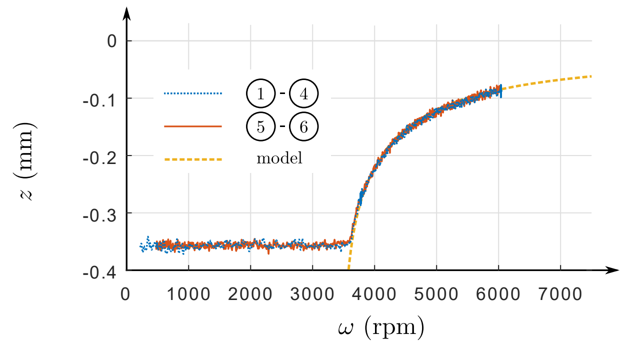

Fig. 12: Evolution of the rotor axial position z with its spin speed ω along the six-step sequence.

the landing bearing and starts to levitate, stabilising around $z = -0.275$ (mm) at 3750 (rpm). The rotor weight thus solely distributes between the load relieving and electrodynamic forces. Throughout step 3, the spin speed ω increases and so does the total axial stiffness $k_{z,t}$, as will be shown in Section VI-C2, implying that the rotor approaches its nominal position, i.e. $z = 0$. As a result, the electrodynamic force F_z drops at the expense of the load relieving one, reaching 95 (g) around $z = -0.085$ (mm) at 6000 (rpm), as illustrated in step 4. Starting from step 5, the AC driver is disconnected from the armature winding, preventing the circulation of the motor currents I_M whereas the suspension currents I_S continue to flow, as in a classic EDTB. In this way, the axial magnetic suspension is still ensured even if the rotor decelerates due to the aerodynamic and electrodynamic drag torques, moving away even further from its equilibrium position. Hence, the electrodynamic effects intensifies to compensate for the load relieving force reduction until the rotor lands on the dedicated bearing. Finally, step 6 exhibits the reverse behaviour with respect to the first one, the electrodynamic force F_z diminishing with the speed ω up to be equal to zero and the contact force $F_{z,n}$ increasing from zero, while the axial position z and thus the sum of these forces do not vary.

The rotor axial speed $\dot{z}$ and acceleration $\ddot{z}$ remaining low all over the six steps, the machine can be considered as operating in quasi-static conditions. Consequently, as expected, the resultant $F_{z,t}$ of the three forces is constant and equal to the rotor weight, endorsing the expression (3) that predicts the electrodynamic force F_z. In the same way, Fig. 12 depicts the evolution of the rotor axial position z with the spin speed ω, the dotted and solid lines corresponding respectively to steps 1-4, linked to the self-bearing operation, and 5-6, related to the thrust bearing functioning, whereas the dashed line to the theoretical position obtained by solving the axial mechanical equation under quasi-static conditions. The consistency between them confirms the independence of the axial suspension to the motor currents I_M and corroborates the electromechanical model given in (2).

2) Axial Stiffness: Fig. 13 represents the evolution of the axial stiffnesses acting on the rotor with the spin speed ω so as to analyse the machine axial static stability. The

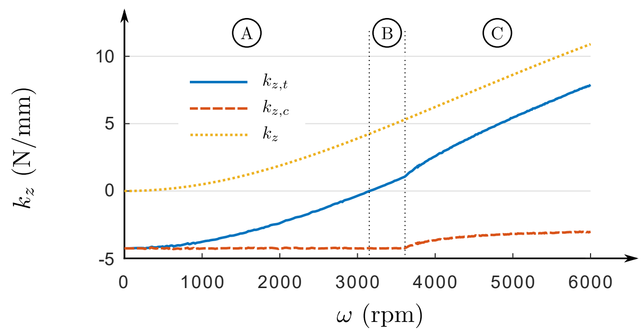

Fig. 13: Evolution of the axial stiffnesses k_z with the rotor spin speed ω throughout the sequence.

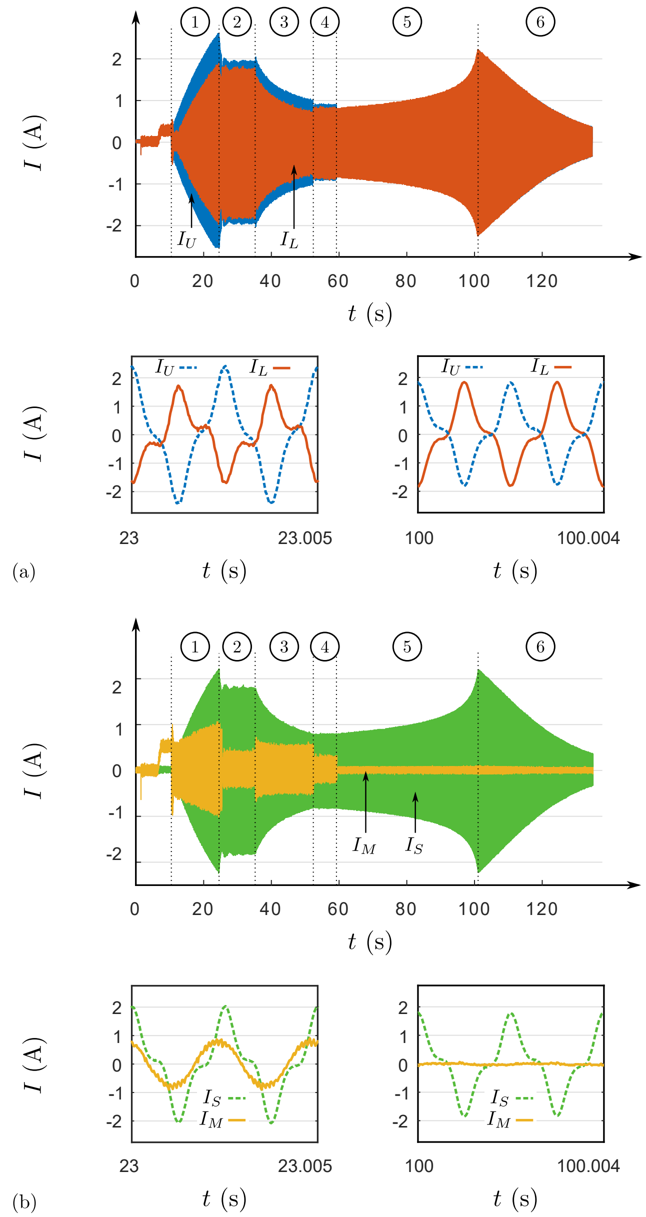

Fig. 14: Time evolution of the currents flowing in phase C throughout the sequence. (a) Currents I_U and I_L flowing respectively in the upper and lower windings. (b) Corresponding suspension current I_S and motor current I_M.

dotted line corresponds to the electrodynamic contribution k_z, calculated through the theoretical expression (3) with the parameters identified above, the dashed line to the destabilising contribution $k_{z,c}$ arising from the permanent magnet bearings, retrieved from the measurement of the axial position z, and the solid line to the resulting total stiffness $k_{z,t}$, namely the sum of both these contributions. Along the speed range considered in this study, three different zones can be identified. In zone A, the total stiffness being negative due to the centring bearing contribution $k_{z,c}$ equal to -4.2 (N/mm), the axial motion suffers from a static instability. The latter disappears as soon as the electrodynamic effects overcome the destabilising stiffness, namely for the rotor spin speed ω_1 defined in (10) and being equal to 3150 (rpm). In zone B, although the axial degree of freedom is stable, the rotor still lies on the lower landing bearing. Indeed, as depicted in Fig. 11, the electrodynamic force F_z is not yet high enough to support the load within the allowed rotor displacement range. Finally, in zone C, that starts from 3600 (rpm), i.e. the speed threshold beyond which fully passive levitation is achieved, the total axial stiffness $k_{z,t}$ increases up to reach 8 (N/mm) at 6000 (rpm). It is worth noting that the spin speed has an indirect but positive impact on the destabilising stiffness $k_{z,c}$, the latter varying from -4.2 to -3 (N/mm), since its absolute value reduces when the rotor gets closer to the EDTSB machine nominal position. Unfortunately, in accordance with Earnshaw's Theorem, the corresponding positive radial stiffness $k_{q,c}$ has to follow the same tendency, diminishing from 2.1 to 1.5 (N/mm).

3) Currents: Fig. 14(a) illustrates the time evolution of the currents I_U and I_L flowing respectively in the upper and lower windings of phase C throughout the whole sequence as well as detailed views retrieved from steps 1 and 5. As expected, during steps 1-4, related to the self-bearing operation, these two currents differ in amplitude due to the contribution of the suspension current I_S. By contrast, in the last two steps, they are equal but of opposite signs since only the suspension current I_S circulates in these windings and, specifically, in the short-circuited path formed by their series connection.

Fig. 14(b) represents the time evolution of the corresponding suspension current I_S and motor current I_M, calculated through (1). First, it should be noted that the suspension current I_S follows a pattern similar to the axial electrodynamic force F_z, described in Section VI-C1, that results from it. Regarding the motor function, before the machine start-up, the sensorless driver performs a step of direct-axis motor current $I_{M,d}$ to estimate the winding resistance. Thereafter, even if the rotor acceleration is constant during step 1, the motor current I_M rises with the spin speed ω as the aerodynamic and, more importantly, the electrodynamic drag torques increase. As soon as the rotor takes off from the landing bearing, the electrodynamic torque $T_{\alpha,D}$ lowers due to its quadratic dependence to the axial position and so does the motor current I_M. The decrease is even more important since, in step 2, no additional current is required to accelerate the rotor, the speed

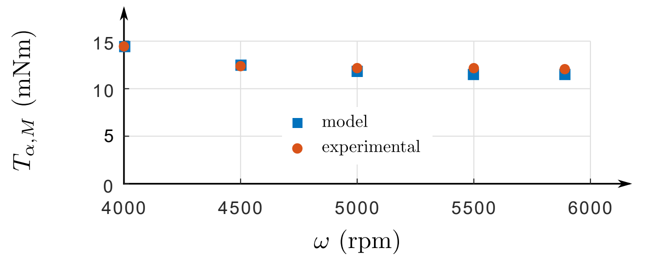

Fig. 15: Evolution of the motor torque $T_{\alpha,M}$ with the rotor spin speed ω along step 3.

being fixed to 3750 (rpm). During step 3, even though the rotor gets closer to its nominal position, the motor current I_M marginally reduces in comparison with the suspension current I_S. Indeed, as will be shown in Section VI-C5, at higher speeds, the aerodynamic effects raise, compensating for and even exceeding the diminution of the electrodynamic torque. The transition to step 4 leads the motor current I_M to drop due to the absence of acceleration. During the last two steps, the AC driver being disconnected, no motor current I_M flows in the armature winding. Finally, let us point out that, unlike its motor counterpart, the suspension current I_S exhibits a significant third harmonic. Although the latter produces a positive electrodynamic stiffness, its contribution is negligible in comparison with that of the fundamental [33]. Hence, this harmonic solely generates Joule losses.

4) Motor Torque: The thrust self-bearing motor under study generates the drive torque $T_{\alpha,M}$ in addition to the passive axial suspension force F_z. This torque can be retrieved from the electromechanical model (2) and, assuming that the direct-axis motor current $I_{M,d}$ is properly regulated to zero, expressed as:

$$T_{\alpha,M} = pK_\alpha \frac{N}{2} I_M, \tag{15}$$

where I_M is the amplitude of the motor current. As expected, it corresponds to the conventional torque expression of a permanent magnet motor. The drive torque $T_{\alpha,M}$ can also be evaluated experimentally by comparing the time evolution of the rotor spin speed in self-bearing machine and thrust bearing operations. More precisely, the total torque exerted on the rotor throughout step 3, calculated through the spin acceleration and the polar moment of inertia J_p, comprises the motor torque $T_{\alpha,M}$ as well as the drag torque, the latter including both the electrodynamic and aerodynamic contributions. By contrast, in step 5, this total torque reduces to its drag component, which is, for each speed ω, equal to that acting in step 3 since the axial position is identical. An experimental evaluation of the motor torque can therefore be obtained by combining the results of both these steps. Fig. 15 shows the evolution of the drive torque $T_{\alpha,M}$ with the spin speed ω along step 3, the square corresponding to the theoretical expression (15) with the measured motor current and the dots to the experimental identification. The deviations between them do not exceed 5.5%, thus validating the motor equations of the model.

5) Drag Losses: The power dissipated in the form of Joule losses by the passively induced suspension current I_S, lying

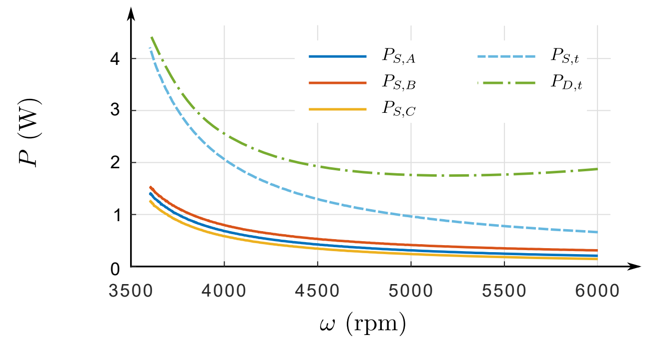

Fig. 16: Evolution of the drag losses with the spin speed ω.

at the basis of the rotor axial levitation, originates from the mechanical power absorbed by the thrust bearing function through the electrodynamic drag torque $T_{\alpha,D}$ [28]. As a result, for each of the three phases, the corresponding drag losses, also referred to as the suspension power consumption P_S, can be calculated based on the measurement of the current I_S and the resistance $2R$ of the short-circuited path formed by the series connection of the upper and lower windings within which this current circulates. Fig. 16 depicts the evolution of the drag losses with the rotor spin speed ω. The solid lines relate to the suspension power consumptions P_S of phases A, B and C, the dashed line to their sum $P_{S,t}$ and the dash-dotted line to the total drag losses $P_{D,t}$, encompassing both the electrodynamic and aerodynamic effects, retrieved from the rotor spin speed deceleration throughout step 5. As already reported in [33], the suspension losses related to each phase differ due to small deviations between their respective equilibrium positions. Indeed, the armature winding being not placed in a ferromagnetic circuit, its geometric precision has a significant impact on the permanent magnet flux linkage. Even though these deviations lead to an augmentation of the drag losses, they do not affect the total electrodynamic force and therefore the passive levitation. Moreover, as expected, the losses related to each of the three phases decrease with the spin speed ω since the rotor approaches its nominal position, the total suspension power consumption $P_{S,t}$ varying from 4 (W) at 3600 (rpm) to 660 (mW) at 6000 (rpm). Finally, the total drag losses $P_{D,t}$ decline with the speed, following the trend pursued by the suspension power consumption, until the aerodynamic effects start to dominate around 5200 (rpm). Beyond this speed, the total losses increase up to reach 1.875 (W) at 6000 (rpm). It is worth noting that these windage losses do not exist when the wheel operates in space.

D. Axial Disturbance

Fig. 17 illustrates the time evolution of the rotor axial position z following an impulse disturbance at several spin speeds ω ranging from 3750 to 5000 (rpm). As expected, the axial natural frequency increases with the speed since the total stiffness $k_{z,t}$ improves thanks to the electrodynamic effects. In contrast, the damping reduces given that the electrodynamic contribution, arising from the component of the suspension

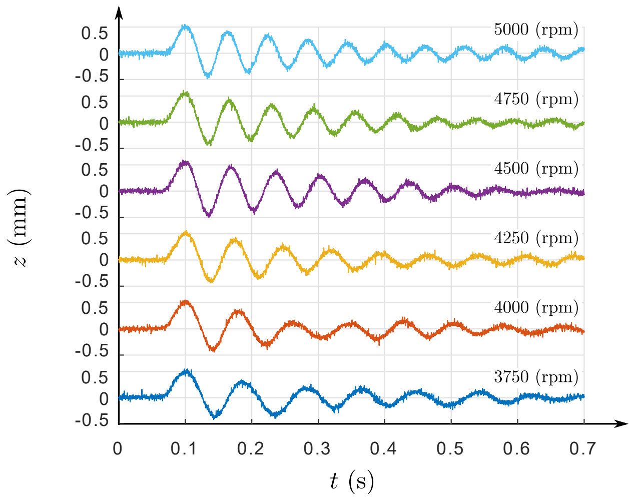

Fig. 17: Time evolution of the rotor axial position z following an impulse axial disturbance at several spin speeds.

current I_S induced by the axial motion, diminishes with the speed ω, as concluded from the analytical model in [32, 36].

E. Improved Centring Bearing Adjustment

As stated in Section VI-B, the axial offsets that separate both rings of each centring bearing have been set so as to only partially counterbalance the rotor weight, thus facilitating the force and current analysis performed hereinabove. However, the remainder of the axial load being supported by the thrust self-bearing machine, this specific adjustment leads to high suspension currents I_S that result in a significant power consumption $P_{S,t}$. Let us briefly study a bearing configuration offering a higher rotor weight compensation. As illustrated in Fig. 18, the load relieving force being increased and the destabilising stiffness $k_{z,c}$ decreased, the spin speed threshold beyond which the rotor starts to levitate is reduced to approximately 2350 (rpm). Besides, as expected, the Joule losses related to each of the three phases and the resulting total power consumption $P_{S,t}$ are lower regardless of the spin speed ω since the rotor is closer to its equilibrium. Unlike the previous bearing adjustment, these losses increase with the spin speed ω from about 4100 (rpm), attaining 190 (mW) at 5950 (rpm), as the rotor axial position z no longer vary significantly.

F. Radial Stability

Although the radial suspension is achieved by PM bearings, radial instabilities with slow dynamics have been noticed for adjustments of their axial offsets providing very low weight compensations and thus leading the rotor to levitate far from the EDTSB machine axial nominal position. In these specific conditions, the flux linked by the armature winding may exhibit a slight dependence to the rotor radial position, with the result that the self-bearing machine also behaves as an electrodynamic centring bearing. Due to the absence of radial damping and the low radial stiffness, this effect may result in the observed dynamic instability issues, as predicted in [19].

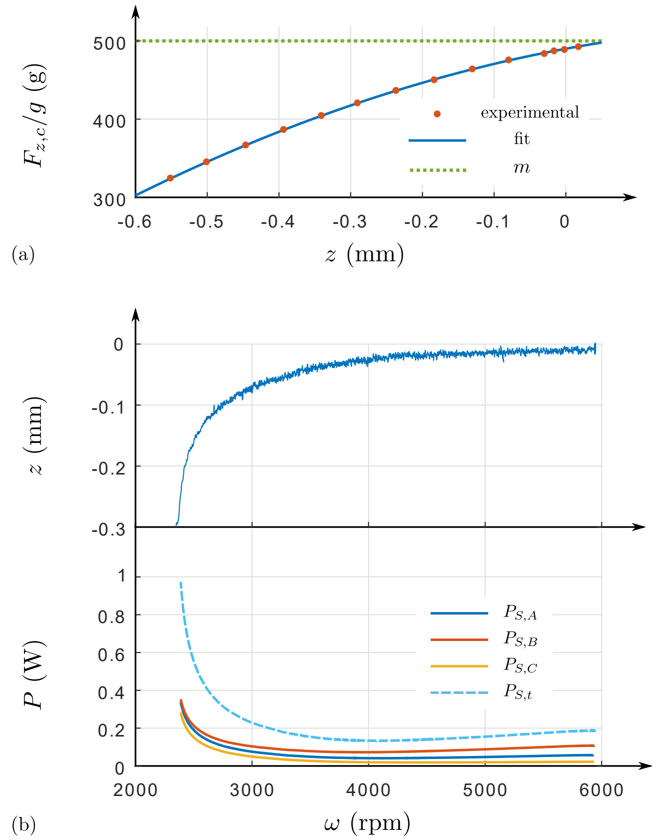

Fig. 18: Improved centring bearing adjustment. (a) Evolution of the axial load relieving force $F_{z,c}$ with the axial position z. (b) Evolution of the axial position z and suspension power consumption $P_{S,t}$ with the spin speed ω.

VII. Conclusion

This paper presents the design, optimisation and experimental characterisation of a reaction wheel implementing the first fully passively levitated self-bearing machine. The rotor radial and tilt stabilisations are ensured by two permanent magnet centring bearings whereas an electrodynamic thrust self-bearing machine provides, through a single multifunction winding, both the motor and passive axial suspension functions. As a result, no sensor, controller and power electronics are required to achieve the levitation, thus increasing the machine compactness and reliability, while the motor function can be operated through a classic driver.

The reaction wheel is sized following an optimal approach leaning on the minimisation of the mass and the losses through an NSGA-II algorithm, each individual being evaluated on the basis of an electromechanical model describing the rotor dynamics and whose parameters are identified through static finite element simulations and analytical formulas. The resulting prototype and the dedicated test rig allowing us to analyse the fully passive suspension are described. Extensive experimental investigations covering the axial forces arising from the centring bearings and the thrust self-bearing machine, the consequent rotor axial position as well as the drive torque corroborate the dynamic model under quasi-static conditions and prove that stable levitation can be carried out solely relying on passive phenomena. Finally, the motor and suspension currents, that are deduced from those flowing within the upper and lower windings, are studied, revealing that suspension power consumption as low as 200 (mW) can be reached at 6000 (rpm) through an efficient rotor weight compensation.

References

[1] T. Tezuka, N. Kurita, and T. Ishikawa, "Design and simulation of a five degrees of freedom active control magnetic levitated motor," *IEEE Transactions on Magnetics*, vol. 49, no. 5, pp. 2257–2262, May 2013.

[2] T. Baumgartner, R. M. Burkart, and J. W. Kolar, "Analysis and design of a 300-w 500 000-r/min slotless self-bearing permanent-magnet motor," *IEEE Trans. Ind. Elec.*, vol. 61, no. 8, pp. 4326–4336, Aug 2014.

[3] M. Osa, T. Masuzawa, T. Saito, and E. Tatsumi, "Magnetic levitation performance of miniaturized magnetically levitated motor with 5-dof active control," *Mech. Eng. Journal*, vol. 4, no. 5, pp. 17–00 007, 2017.

[4] A. Tuysuz, T. Achtnich, C. Zwyssig, and J. Kolar, "A 300 000-r/min magnetically levitated reaction wheel demonstrator," *IEEE Transactions on Industrial Electronics*, vol. 66, no. 8, pp. 6404–6407, Aug. 2019.

[5] R. Schoeb and N. Barletta, "Principle and application of a bearingless slice motor," *JSME Int. J. Series C*, vol. 40, no. 4, pp. 593–598, 1997.

[6] B. Warberger, R. Kaelin, T. Nussbaumer, and J. W. Kolar, "50-nm/2500-w bearingless motor for high-purity pharmaceutical mixing," *IEEE Trans. Ind. Elec.*, vol. 59, no. 5, pp. 2236–2247, May 2012.

[7] H. Mitterhofer, B. Mrak, and W. Gruber, "Comparison of high-speed bearingless drive topologies with combined windings," *IEEE Transactions on Industry Applications*, vol. 51, no. 3, pp. 2116–2122, May 2015.

[8] P. Puentener, M. Schuck, D. Steinert, T. Nussbaumer, and J. W. Kolar, "A 150 000-r/min bearingless slice motor," *IEEE/ASME Transactions on Mechatronics*, vol. 23, no. 6, pp. 2963–2967, Dec 2018.

[9] Q. D. Nguyen and S. Ueno, "Analysis and control of nonsalient permanent magnet axial gap self-bearing motor," *IEEE Transactions on Industrial Electronics*, vol. 58, no. 7, pp. 2644–2652, July 2011.

[10] J. Asama, Y. Hamasaki, T. Oiwa, and A. Chiba, "Proposal and analysis of a novel single-drive bearingless motor," *IEEE Transactions on Industrial Electronics*, vol. 60, no. 1, pp. 129–138, Jan 2013.

[11] W. Bauer and W. Amrhein, "Electrical design considerations for a bearingless axial-force/torque motor," *IEEE Transactions on Industry Applications*, vol. 50, no. 4, pp. 2512–2522, July 2014.

[12] H. Sugimoto, S. Tanaka, A. Chiba, and J. Asama, "Principle of a novel single-drive bearingless motor with cylindrical radial gap," *IEEE Trans. Ind. App.*, vol. 51, no. 5, pp. 3696–3706, Sept 2015.

[13] H. Sugimoto, I. Shimura, and A. Chiba, "A novel stator structure for active axial force improvement in a one-axis actively positioned single-drive bearingless motor," *IEEE Transactions on Industry Applications*, vol. 53, no. 5, pp. 4414–4421, Sept 2017.

[14] S. Earnshaw, "On the nature of the molecular forces which regulate the constitution of the luminiferous ether," *Transactions of the Cambridge Philosophical Society*, vol. 7, pp. 97–112, 1839.

[15] N. Amati, X. D. Lepine, and A. Tonoli, "Modeling of electrodynamic bearings," *Journal of Vibration and Acoustics*, vol. 130(6), 2008.

[16] A. Tonoli, N. Amati, F. Impinna, and J. G. Detoni, "A solution for the stabilization of electrodynamic bearings: Modeling and experimental validation," *Journal Vib. and Acoustics*, vol. 133, no. 2, p. 021004, 2011.

[17] J. G. Detoni, F. Impinna, A. Tonoli, and N. Amati, "Unified modelling of passive homopolar and heteropolar electrodynamic bearings," *Journal of Sound and Vibration*, vol. 331, no. 19, pp. 4219 – 4232, 2012.

[18] J. G. Detoni, "Progress on electrodynamic passive magnetic bearings for rotor levitation," *Proceedings of the Institution of Mechanical Engineering, Part C: Journal of Mechanical Engineering Science*, vol. 228, no. 10, pp. 1829–1844, 2014.

[19] C. Dumont, V. Kluyskens, and B. Dehez, "Linear state-space representation of heteropolar electrodynamic bearings with radial magnetic field," *IEEE Transactions on Magnetics*, vol. 52, no. 1, pp. 1–9, Jan 2016.

[20] V. Kluyskens, J. Van Verdeghem, and B. Dehez, "Experimental investigations on self-bearing motors with combined torque and electrodynamic bearing windings," *Actuators*, vol. 8, no. 2, 2019.

[21] J. G. Detoni, F. Impinna, N. Amati, and A. Tonoli, "Stability of a four-degree-of-freedom rotor on homopolar electrodynamic passive magnetic bearings," *Proc. of the Inst. of Mech. Eng., Part I: Journal of Systems and Control Engineering*, vol. 230, no. 4, pp. 330–338, 2016.

[22] N. Amati, F. Impinna, J. G. Detoni, and A. Tonoli, "Test and theory of electrodynamic bearings coupled to active magnetic dampers," *Proceedings of the Institution of Mechanical Engineers, Part I: Journal of Systems and Control Engineering*, vol. 230, no. 8, pp. 706–715, 2016.

[23] K. D. Bachovchin, J. F. Hoburg, and R. F. Post, "Magnetic fields and forces in permanent magnet levitated bearings," *IEEE Transactions on Magnetics*, vol. 48, no. 7, pp. 2112–2120, July 2012.

[24] H. B. J. Sandtner, "Compact passive electrodynamic thrust bearing," in *11th International Symposium on Magnetic Bearings*, 2008.

[25] J. Van Verdeghem, V. Kluyskens, and B. Dehez, "Optimisation and comparison of axial flux and radial flux electrodynamic thrust bearings," in *2nd IEEE Advance In Magnetics (AIM)*, 2018.

[26] J. Sandtner and H. Bleuler, *Electrodynamic passive magnetic bearing with planar halbach arrays*. Lexington, USA: Proceedings of the Ninth Internation Symposium on Magnetic Bearings, 2004.

[27] K. D. Bachovchin, J. F. Hoburg, and R. F. Post, "Stable levitation of a passive magnetic bearing," *IEEE Transactions on Magnetics*, vol. 49, no. 1, pp. 609–617, Jan 2013.

[28] F. Impinna, J. G. Detoni, N. Amati, and A. Tonoli, "Passive magnetic levitation of rotors on axial electrodynamic bearings," *IEEE Transactions on Magnetics*, vol. 49, no. 1, pp. 599–608, Jan 2013.

[29] J. Van Verdeghem, C. Dumont, V. Kluyskens, and B. Dehez, "Linear state-space representation of the axial dynamics of electrodynamic thrust bearings," *IEEE Trans. Mag.*, vol. 52, no. 10, pp. 1–12, Oct 2016.

[30] J. Van Verdeghem, V. Kluyskens, and B. Dehez, "Five degrees of freedom linear state-space representation of electrodynamic thrust bearings," *Journal of Sound and Vibration*, vol. 405, pp. 48 – 67, 2017.

[31] H. K. Asper and S. Siposs, *Passive Magnetic bearing with integrated motor generator for flywheel applications*. Dresden, Germanny: 8th International Symposium On Magnetic Suspension Technology, 2005.

[32] J. Van Verdeghem, M. Lefebvre, V. Kluyskens, and B. Dehez, "Dynamical modeling of passively levitated electrodynamic

thrust self-bearing machines," *IEEE Transactions on Industry Applications*, vol. 55, no. 2, pp. 1447–1460, March 2019.

[33] J. Van Verdeghem, V. Kluyskens, and B. Dehez, "Experimental investigations on passively levitated electrodynamic thrust self-bearing motors," *IEEE Transactions on Industry Applications*, vol. 55, no. 5, pp. 4743–4753, Sep. 2019.

[34] J. Van Verdeghem and B. Dehez, "Experimental characterisation of tilt stabilisation within passively levitated electrodynamic thrust self-bearing motors," in *2019 IEEE International Electric Machines Drives Conference (IEMDC)*, May 2019, pp. 812–819.

[35] ——, "Fully passively levitated self-bearing machines with combined windings," in *2020 IEEE Energy Conversion Congress and Exposition (ECCE)*, 2020, pp. 254–261.

[36] J. Van Verdeghem, V. Kluyskens, and B. Dehez, "Stability and performance analysis of electrodynamic thrust bearings," *Actuators*, vol. 8, no. 1, 2019.

[37] P. Pfister and Y. Perriard, "A 200 000 rpm, 2 kw slotless permanent magnet motor," in *2008 International Conference on Electrical Machines and Systems*, Oct 2008, pp. 3054–3059.

Joachim Van Verdeghem (S'18-M'21) received the Master and Ph.D. degrees in electromechanical engineering from the Université catholique de Louvain (UCLouvain), Louvain-la-Neuve, Belgium, in 2016 and 2020 respectively.

From February to May 2020, he was a Visiting Scholar at the University of Wisconsin-Madison, Madison, WI, USA, where he worked on bearingless motors with the Wisconsin Electric Machines and Power Electronics Consortium (WEMPEC). He is currently a Research Fellow at the Mechatronic, Electrical Energy, and Dynamic systems (MEED) department, Université catholique de Louvain (UCLouvain). His research interests include magnetic bearings and bearingless motors, with a focus on passively levitated systems.

Bruno Dehez (SM'17) received the Master degree in electromechanical engineering and the Ph.D. degree from the Université catholique de Louvain (UCLouvain), Louvain-la-Neuve, Belgium, in 1998 and 2004, respectively.

He is currently a Professor at the Ecole Polytechnique de Louvain (EPL) and is Head of the Mechatronic, electrical energy, and dynamic systems (MEED) department, Université catholique de Louvain (UCLouvain). His research interests are in the field of design and optimization of electromagnetic devices, and particularly of electrical machines and actuators.